Earth and Planetary Science Letters 457 (2017) 412–422

Contents lists available at ScienceDirect

Earth and Planetary Science Letters

www.elsevier.com/locate/epsl

Late quaternary climate, precipitation $\delta^{18}O$, and Indian monsoon variations over the Tibetan Plateau

Jingmin Li [a,c], Todd A. Ehlers [a,*], Martin Werner [b], Sebastian G. Mutz [a], Christian Steger [c], Heiko Paeth [c]

[a] Dept. of Geosciences, Univ. of Tübingen, Germany
[b] Climate Science Division, Alfred Wegener Institute, Germany
[c] Institute of Geography and Geology, Univ. of Würzburg, Germany

ARTICLE INFO

Article history:
Received 19 February 2016
Received in revised form 16 September 2016
Accepted 21 September 2016
Available online 4 November 2016
Editor: A. Yin

Keywords:
Tibet
precipitation $\delta^{18}O$
monsoon intensity
mid-Holocene
Last Glacial Maximum
GCM

ABSTRACT

The Himalaya–Tibet orogen contains one of the largest modern topographic and climate gradients on Earth. Proxy data from the region provide a basis for understanding Tibetan Plateau paleo climate and paleo elevation reconstructions. Paleo climate model comparisons to proxy data compliment sparsely located data and can improve climate reconstructions. This study investigates temporal changes in precipitation, temperature and precipitation $\delta^{18}O$($\delta^{18}O_p$) over the Himalaya–Tibet from the Last Glacial Maximum (LGM) to present. We conduct a series of atmospheric General Circulation Model (GCM, ECHAM5-wiso) experiments at discrete time slices including a Pre-industrial (PI, Pre-1850 AD), Mid Holocene (MH, 6 ka BP) and LGM (21 ka BP) simulations. Model predictions are compared with existing proxy records. Model results show muted climate changes across the plateau during the MH and larger changes occurring during the LGM. During the LGM surface temperatures are ~2.0–4.0 °C lower across the Himalaya and Tibet, and >5.0 °C lower at the northwest and northeast edge of the Tibetan Plateau. LGM mean annual precipitation is 200–600 mm/yr lower over on the Tibetan Plateau. Model and proxy data comparison shows a good agreement for the LGM, but large differences for the MH. Large differences are also present between MH proxy studies near each other. The precipitation weighted annual mean $\delta^{18}O_p$ lapse rate at the Himalaya is about 0.4‰/km larger during the MH and 0.2‰/km smaller during the LGM than during the PI. Finally, rainfall associated with the continental Indian monsoon (between 70°E–110°E and 10°N–30°N) is about 44% less in the LGM than during PI times. The LGM monsoon period is about one month shorter than in PI times. Taken together, these results document significant spatial and temporal changes in temperature, precipitation, and $\delta^{18}O_p$ over the last ~21 ka. These changes are large enough to impact interpretations of proxy data and the intensity of the Indian monsoon.

1. Introduction

Paleo climate and paleo environmental proxy records from the Tibetan Plateau and its surrounding areas provide a basis for reconstructing Tibetan Plateau climate change and paleo-elevation reconstructions. Proxy records are reconstructed from different types of materials (e.g., fossils; lacustrine, aeolian, and glacial sediments; soil carbonates; vegetation and pollen) which contain different elements and isotopes (e.g., O, C, H, etc.). These records are often used to document changes in precipitation and temperature. Tibetan proxy records have previously been used to reconstruct paleo climate ranging from the Early Cenozoic (~50 Ma; e.g. Graham et al., 2005; Kent-Corson et al., 2009) to Late Quaternary (~2.1 ka BP to present; e.g. Herzschuh et al., 2006). A growing number of proxy studies come from Late Quaternary lacustrine sediments and ice cores, and are used to investigate recent climate change on the Tibetan Plateau (see data compilation in supplemental Tables S1, S2). Most existing studies contain records of Holocene variations, and a few records extend back to the Last Glacial Maximum. Interestingly, results from previous observational records indicate large spatial and temporal variations in climate relative to the modern, but with the shortcoming that it is difficult to extrapolate between individual study areas and to understand the natural spatial variability that could be present across the plateau. This study addresses this shortcoming using an isotope-tracking GCM.

* Corresponding author.
E-mail address: todd.ehlers@uni-tuebingen.de (T.A. Ehlers).

http://dx.doi.org/10.1016/j.epsl.2016.09.031
0012-821X/

Previous paleoclimate reconstructions from observational records on the Tibetan Plateau indicate a large degree of spatial variation in plateau climate and precipitation $\delta^{18}O(\delta^{18}O_p)$. For example, MH proxy records from sediment cores in Cuoe Lake in central Tibet (Wu et al., 2006) and Zabuye Lake in western Tibet (Wang et al., 2002) suggested a warm and wetter MH climate than today. Proxy studies from Lake Kuhai in the northeastern Tibetan Plateau (Wischnewski et al., 2011) and Ahung Co Lake in central Tibet (Morrill et al., 2006) suggested drier MH conditions. However, some MH climate reconstructions from the Tibetan Plateau are inconsistent with each other. Disagreements between MH climate reconstructions exist in records from the same, and neighboring, geographic locations. For example, two nearby lakes (Sumxi Co and Lake Bangong) in western of Tibet, Gasse et al. (1991) suggested warm and wetter MH conditions than present, whereas Van Campo et al. (1996) suggested drier conditions than present. In contrast to the MH, LGM climate reconstructions from previous Tibetan Plateau studies provide a more consistent picture of the paleo precipitation and temperature distribution (e.g. Kotlia et al., 2010; Hodell et al., 1999; Herzschuh et al., 2006; Wang et al., 2002). Previous studies document a colder and drier than modern climate across Tibet except one study that suggests colder LGM conditions, but similar precipitation as today, in Eastern Nepal (Asahi, 2010). Thus, despite the advances of previous studies, they leave some uncertainty concerning the spatial and temporal variations in Late Quaternary Tibetan climate, and warrant alternative approaches to understand climate change in the region.

The complex spatial distribution in oxygen isotopes over the Tibetan Plateau region has been also observed from direct precipitation measurements of modern $\delta^{18}O_p$ (e.g. Tian et al., 2007; Yao et al., 2013) and also within stream water (Hren et al., 2009). Those studies suggest a strong temperature effect on $\delta^{18}O_p$ in the northeast of the Tibetan Plateau and a strong precipitation amount effect in the middle and south of the Tibetan Plateau. Beside the $\delta^{18}O_p$ isotope distribution, another variable investigated here is the $\delta^{18}O_p$ isotope lapse rate. It is often used for climate reconstructions and for estimates of the paleo elevation of an orogen (e.g. Chamberlain and Poage, 2000), but it varies with climate and environment. Elevation reconstructions based on modern $\delta^{18}O_p$ isotope lapse rate may contain climatic uncertainties that overwhelm the elevation signal (e.g. Ehlers and Poulsen, 2009).

Understanding the spatial and temporal variations in climate, $\delta^{18}O_p$, and the driving forces for these changes requires a systematic investigation of the relevant processes active at different time intervals. Atmospheric GCMs provide one means of investigating spatial variations in paleoclimate at specific time slices. For example, Dallmeyer and Claussen (2011) investigate precipitation changes from the MH to modern in the Asian monsoon region using the coupled ECHAM5/JSBACH model. They found that precipitation changes in the East Asian monsoon region are not only dependent on changes in the Indian summer monsoon circulation, but also on changes in the mid-latitudinal westerly winds that dominate circulation during the pre-monsoon season. Zheng et al. (2004) conducted paleo climate time slice experiments at 6 ka BP and 21 ka BP for the East Asian Monsoon region using a regional climate model (RegCM2) with detailed land surface processes. Their results show the East Asian summer monsoon strengthening, a precipitation increase, and a shift of the monsoon rain belt westwards and northwards during the MH. They also demonstrated a winter monsoon strengthening due to low atmospheric temperatures during the LGM. Despite these advances, the previous studies do not provide estimates for proxy records such as $\delta^{18}O_p$ because isotope-tracking GCMs were not used.

In the past decade, isotope-tracking GCMs have become a powerful tool for understanding the interactions of different Earth systems and variations in $\delta^{18}O_p$ (e.g. Feng et al., 2013). This study presents results from an isotope-tracking GCM (ECHAM5-wiso) for two paleo time slices including the Middle Holocene (MH, 6 ka BP) and Last Glacial Maximum (LGM, 21 ka BP). These two time slices are combined with a simulation of Pre-Industrial (PI, Pre-1850 AD) conditions to capture temperature and precipitation, and $\delta^{18}O_p$ variations during the most recent glacial–interglacial cycle. We complement previous model work by (1) investigating climate change using time-specific boundary conditions for the MH and LGM, and (2) evaluating changes in $\delta^{18}O_p$ in the MH and LGM. We investigate these changes in comparison to Pre-Industrial (PI) conditions. In the following, we present spatial and seasonal variation in temperature, precipitation, $\delta^{18}O_p$, and the $\delta^{18}O_p$ lapse rate for all time slices. We compare model predictions with proxy data, interpret variations in the monsoon duration and intensity, and identify the climate controls $\delta^{18}O_p$ over the Tibetan Plateau. Finally, GCM predictions of $\delta^{18}O_p$ are compared to the simpler approach of a 1D Rayleigh Distillation Model (RDM) to assess if this simpler approach captures the relevant past and present fractionation processes active in the high-relief areas surrounding the Tibetan Plateau.

2. Model setup and methods

2.1. Model setup for different time slices

Climate and $\delta^{18}O_p$ variation over the Tibetan Plateau are investigated using an atmospheric general circulation model equipped with isotope calculation capabilities (ECHAM5-wiso). In this model, water isotopes (HDO, $H_2{}^{16}O$, and $H_2{}^{18}O$, treated as independent tracers) experience kinetic fractionation and equilibrium during phase transitions (e.g. vapor, cloud, snow etc.) in the atmosphere (Werner et al., 2011). Several publications have evaluated its performance and demonstrated a good global and regional agreement of observational data with the simulated isotopic fraction of precipitation (e.g. Werner et al., 2011; Langebroek et al., 2011). In the Tibetan region, Yao et al. (2013) demonstrated that high-resolution atmospheric models (including ECHAM5-wiso) capture the temporal and spatial distribution of water isotope in precipitation.

In this study, simulations are conducted at a resolution of T106L31 (spatial resolution of $1.1^\circ \times 1.1^\circ$, and 31 vertical levels). The simulations are set up with LGM, MH and PI boundary conditions. The simulations are run for >13 model years. Since isotopes are not tracked in subsurface waters, simulations have a short (<2 yr) spin-up time and the last >10 yr are used for analysis. Pre-industrial ocean boundary conditions are taken from the AMIP2 observational climatologic data. MH and LGM sea surface temperatures (SST) and sea ice concentrations (SIC) are derived from the coupled atmosphere–ocean model ECHO-G (Lorenz and Lohmann, 2004) as described in Dietrich et al. (2013). The vegetation boundary for the MH and LGM is constructed from the Paleoclimate Modelling Intercomparison Project (PMIP) Phase II observational data (http://pmip2.lsce.ipsl.fr; Braconnot et al., 2007) and its gaps are filled with vegetation model predictions from Arnold et al. (2009). For the LGM climate, the land–sea distribution, and ice sheet extent and thickness, follow the guidelines of PMIP Phase III (https://pmip3.lsce.ipsl.fr). The green house concentrations and orbital parameter during the PI, MH and LGM are based on table 1 in Dietrich et al. (2013) and from Otto-Bliesner et al. (2006).

2.2. Rayleigh Distillation Model (RDM)

The RDM model is widely used in the observational studies for paleo elevation reconstructions due to its simplicity (e.g. Rowley and Garzione, 2007). The model is based on the conservation of moist static energy. It assumes the condensation of a single air parcel during adiabatic cooling. When an unsaturated air parcel

ascends, it first experiences cooling at the dry adiabatic lapse until its temperature drops to the dew point. Following this, it cools at the moist adiabatic lapse rate. Under the assumption that all condensed vapor precipitates, the remaining vapor fraction and its delta value can be calculated based on the liquid–vapor equilibrium and the estimated temperature and elevation curves. The detailed algorithm used can be found in Rowley and Garzione (2007) and Feng et al. (2013). In this study, RDM $\delta^{18}O_p$ is calculated starting with a GCM-derived moisture source at low elevation (foreland of the Himalaya). The GCM simulated $\delta^{18}O_p$ change with elevation is then compared to the RDM prediction to evaluate the difference between the approaches over the large elevation gradient of the Himalaya.

The GCM predicted $\delta^{18}O_p$ considers more complex physical processes than the RDM. This is because an isotopic counterpart ($H_2{}^{16}O$, $H_2{}^{18}O$ and HDO) for all components of the hydrological cycle (e.g. vapor, cloud, snow and drainage) are treated independently in the GCM prediction and undergo kinetic fractionation and equilibrium during their phase changes in the atmosphere. The isotope effects neglected by the RDM include: e.g. kinetic effects, partial sub-cloud re-evaporation of rain droplets.

2.3. Trajectory analysis for vapor source changes

Lagrangian trajectory analysis is a method for quantifying air mass trajectories that control the transport of $\delta^{18}O$ in a GCM. For the trajectory of a specific infinitesimally small air parcel, the parcel position at a certain time is dependent on the velocity vector of that time and its previous location. Using the GCM predicted 3D wind fields, the backwards trajectories of vapor can be tracked. A comprehensive description of the Lagrangian back trajectory calculation used here can be found in Feng et al. (2013).

The trajectory analysis is applied to the model simulations using 6-hourly model output including the wind velocity in a pressure level system. The wind velocity is linearly interpolated to a 20-min time interval. The target location (i.e. the location where the back trajectory is calculated from) used in this study is in the southeastern Himalaya. This location was selected because it is a potential vapor source for the Tibetan region during the Monsoon season. The wind field is averaged from 100–850 hPa where the water vapor is concentrated. The wind vectors at the target location inside the T106 resolution grid box were interpolated using a bilinear interpolation and tracked backwards for ten days.

3. Results

3.1. Simulated anomalies of temperature, precipitation and $\delta^{18}O_p$

We compare the 10-year mean annual surface temperature, precipitation and $\delta^{18}O_p$ for the three time slices (PI, MH and LGM), and show the results as the difference in values compared to the PI (e.g. MH-PI, LGM-PI). Hereafter, we refer to these differences as the anomalies (relative to PI). A statistical *t*-test is applied to assess the significance of the difference between MH, LGM and PI (Figs. 1–3). Areas that are colored show differences that are significant at the 95% confidence level, the white regions indicate areas where the difference between simulations is resolved at the <95% confidence level and not interpreted.

Simulated PI temperature and MH-LGM temperature anomalies are shown in Fig. 1. Simulated PI temperatures (Fig. 1A) indicate that in the eastern Tibetan Plateau (at longitudes ~>90°E), the mean annual temperature is ~−3.0 to 0.5 °C. Colder temperature are predicted for the southwest plateau (the eastern Himalaya, Na, Fig. 1) and northwest (the Kunlun mountains, KU, Fig. 1) with mean annual temperatures between ~−10 to −7.0 °C. The MH temperature deviates little from the PI temperature conditions on

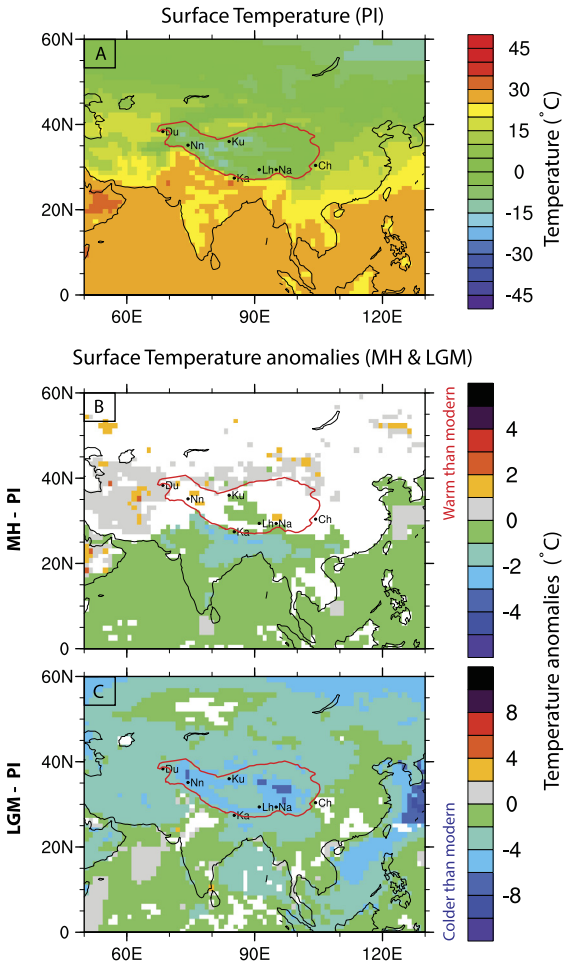

Fig. 1. Simulated annual mean temperature anomalies. (A): simulated PI annual mean temperature. (B) and (C): simulated MH and LGM annual mean temperature anomalies. The differences that are significant below the 95% level are shaded in white. The red line circles the region where elevation exceeds 1500 m. The locations marked here are Du: Dushanbe, Nn: Nanga parbat, Ku: Kunlun Mountains, Ka: Kathandu, Lh: Lhasa, Na: Namcha barwa and Ch: Chengdu. (For interpretation of the references to color in this figure legend, the reader is referred to the web version of this article.)

the plateau. More specifically, during the MH surface temperatures are ~0.5 °C colder on the central Tibetan Plateau, ~1.0 °C colder at the Himalayan front, and ~0.5 °C warmer than PI temperatures over the northern part of the Tibetan Plateau. In contrast, LGM temperatures are typically cooler over the region. During the LGM surface temperatures are ~2.0–6.0 °C cooler across the Himalaya and Tibet, and >6.0 °C cooler in the northwest and southeast edges of the Plateau.

Simulated PI precipitation (Fig. 2A) shows higher values from Dushanbe (>2.0 m/yr, Du Fig. 2A) located west of the Tibetan Plateau and continuing along the Himalaya to the East. The southeast Plateau receives large amounts of precipitation (1.0–2.5 m/yr), whereas the northwest Plateau is drier with precipitation amounts of <0.5 m/yr. Predicted mean annual MH precipitation anomalies show a general trend of wetter conditions in the MH and drier in the LGM compared to PI conditions (Figs. 2B and C). Mean annual MH precipitation is ~<0.1 m/yr wetter on the plateau and 0.3–0.5 m/yr wetter across the Himalaya compared to the PI. During the LGM, mean annual precipitation is 0.2–0.6 m/yr drier over the Tibetan Plateau relative to PI conditions (Fig. 2C). Across the western Himalaya, LGM mean annual precipitation is 0.4–0.8 m/yr drier than the PI. Along the eastern Himalaya, the predicted mean annual precipitation is wetter (>0.8 m/yr) close to Kathandu and

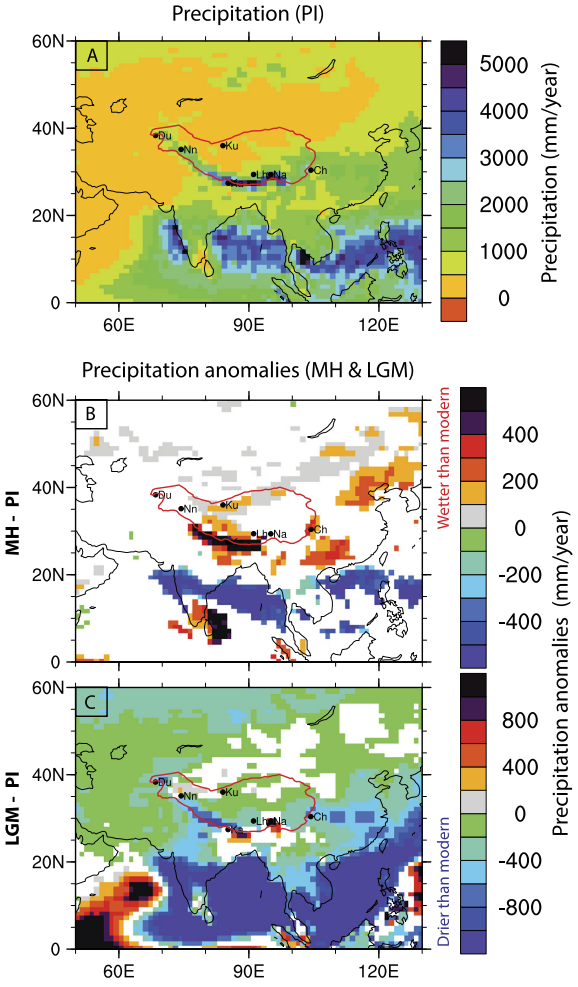

Fig. 2. Simulated annual mean precipitation anomalies. (A): simulated PI annual mean precipitation. (B) and (C): simulated MH and LGM annual mean precipitation anomalies. The differences that are significant below the 95% level are shaded in white. Labels and the red line are the same as in Fig. 1. (For interpretation of the references to color in this figure legend, the reader is referred to the web version of this article.)

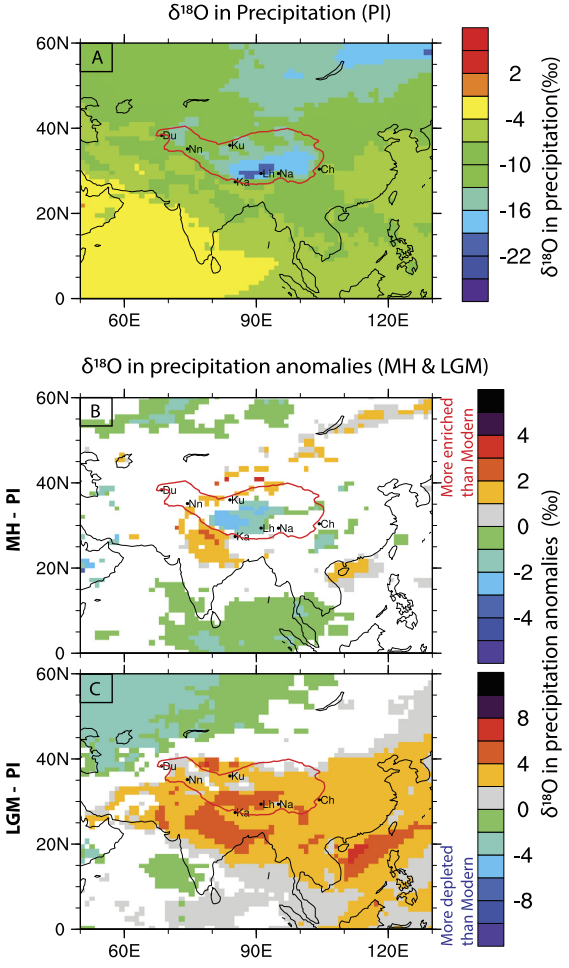

Fig. 3. Simulated annual mean $\delta^{18}O_p$ anomalies. (A): simulated PI annual mean $\delta^{18}O_p$. (B) and (C): simulated MH and LGM annual mean $\delta^{18}O_p$ anomalies. The differences that are significant below the 95% level are shaded in white. Labels and red line are the same as in Fig. 1. (For interpretation of the references to color in this figure legend, the reader is referred to the web version of this article.)

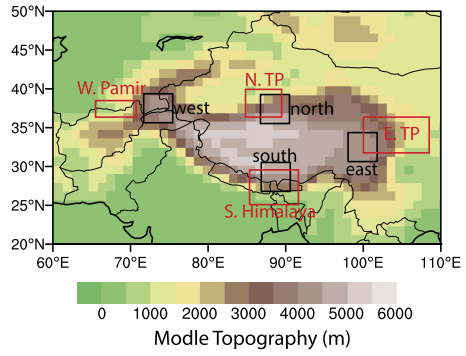

Fig. 4. (1) South, north, west and east regions on the Tibetan Plateau for investigating the variation of $\delta^{18}O_p$ and the climate during the MH and LGM (black boxes: ~350 × 350 km). (2) 4 mountain slopes at the edge of the Tibetan Plateau for isotope lapse rate calculation (red boxes), regions include the south slope of the Himalaya, north slope of the Tibetan Plateau, west slope of the Pamir, east slope of the Tibetan Plateau. (For interpretation of the references to color in this figure legend, the reader is referred to the web version of this article.)

Namcha, but shows no significant change in surrounding areas relative to PI values (white colors in Fig. 2C).

PI $\delta^{18}O_p$ (Fig. 3A) is characterized by a depletion of $\delta^{18}O_p$ from the northwest of the Tibetan Plateau (~−10‰) to the southeast of the Tibetan Plateau (~−19‰). Local lows in $\delta^{18}O_p$ values exist in the Pamir region (−16‰ to −19‰) northwest of the Tibetan Plateau and north of Kathmandu to Lhasa (−19‰ to −22‰) and in the southeast plateau. In comparison to PI conditions, simulated MH $\delta^{18}O_p$ is 1.0‰ depleted on the plateau and 1.0‰ enriched across, and south of, the Himalaya (Fig. 3B). LGM $\delta^{18}O_p$ is 2.0–6.0‰ enriched relative to pre-industrial predictions across the plateau, and continuing eastward to the Pacific Ocean. However, northwest of the plateau, LGM $\delta^{18}O_p$ values go the opposite direction and are more depleted (Fig. 3C). The causes for the $\delta^{18}O_p$ changes will be discussed later in the context of variable vapor source, temperature, precipitation amount, and evaporative recycling.

3.2. Seasonal and spatial variations of $\delta^{18}O_p$, temperature and precipitation

The spatial and seasonal (winter defined as the months DJF, and summer defined as JJA) variations in $\delta^{18}O_p$ and climate were investigated for the MH and LGM. To simplify the presentation of results we focus on four different domains near the edges of the Tibetan Plateau (black boxes in Fig. 4). The size of each domain is 3×3 model grid cells to provide a regional representation. The different domains shown in Fig. 4 are then investigated for variations in $\delta^{18}O_p$, temperature, and precipitation for each of the three time

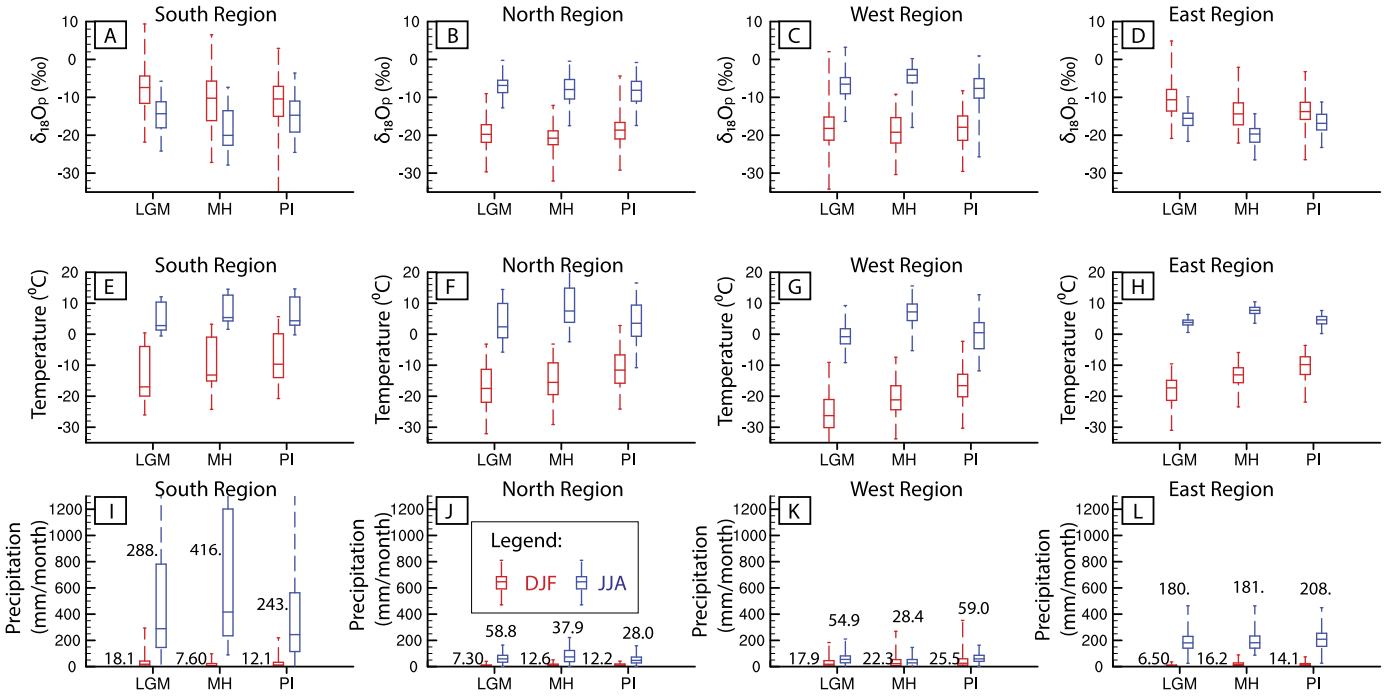

Fig. 5. Box plots for $\delta^{18}O_p$, temperature and precipitation of 2 seasons (DJF and JJA), 4 regions (South, north, west and east) and 3 time slices (LGM, MH and PI). Each box plot represents the maximum, 75pth percentile, median, 25th percentile and minimum value of the variables. The statistical calculations are based on a number of >270 samples (9 grid boxes in each region, 3 months, and >10 simulation years). Winter (DJF) and summer (JJA) results are represented with red and blue boxes respectively. The numbers of the precipitation amount are added to Fig. 5I–L. (For interpretation of the references to color in this figure legend, the reader is referred to the web version of this article.)

slices (PI, MH and LGM). The results provide the following information: (1) Seasonal variations, (2) spatial variations between each region, and (3) paleo to modern variation of $\delta^{18}O_p$, precipitation and temperature. The correlation coefficients of $\delta^{18}O_p$, temperature, and precipitation are not shown here, but will be presented in the next Section 4.3.

The seasonal and spatial variation of $\delta^{18}O_p$, temperature, and precipitation during the LGM, MH and PI are presented in Fig. 5. Each bar-and-whisker plot represents the maximum value, 75th percentile, median, 25 percentile and minimum value of the variables plotted. The statistical calculations are based on >270 values (9 grid boxes in each region, 3 months, and >10 simulation years). Winter (DJF) and summer (JJA) results are presented as red and blue boxes respectively.

The $\delta^{18}O_p$ variations in Figs. 5A–D illustrate several key points. First, for all time slices (LGM, MH and PI), the median $\delta^{18}O_p$ is ~2.0–5.0‰ more enriched during winter than summer for the south and east region (Figs. 5A and D), and is ~10 to −13‰ more depleted during the winter than summer for the northern and western region (Figs. 5B and C). These variations in $\delta^{18}O_p$ indicate that the three $\delta^{18}O_p$ distributions zones (southeast zone, transitional zone, and northwest zones) identified based on the modern day $\delta^{18}O_p$ variability (Yao et al., 2013) also existed during the MH and LGM as well. Second, LGM and MH climate caused a larger (~1.0–5.0‰) difference in median $\delta^{18}O_p$ between the winter and summer across the Tibetan Plateau than during PI climate. In the south region, for example, the seasonal differences are ~6.0‰ in the LGM, ~10‰ in the MH, and ~5.0‰ for the PI simulations (Fig. 5A). Finally (third), the LGM and MH $\delta^{18}O_p$ anomalies show both regional and seasonal variations. In the southern and eastern regions, LGM $\delta^{18}O_p$ is more enriched than PI values for both the winter and summer. The largest enrichment (~4.0‰) is simulated for the eastern region during the winter (Fig. 5D). In the western and northern regions (Figs. 5B and C), the LGM mean $\delta^{18}O_p$ is ~<0.5‰ more depleted in the winter but ~<0.5‰ more enriched in summer. MH $\delta^{18}O_p$ anomalies show a complex trend as well. In the south and eastern regions (Figs. 5A and D), MH $\delta^{18}O_p$ is approximately the same as PI $\delta^{18}O_p$ in the winter, but heavily depleted in the summer (~4.0–6.0‰). In the northern and western regions, MH median $\delta^{18}O_p$ is ~2.0‰ more depleted than the PI median in winter, and ~0.5–4.0‰ more enriched than the PI median in the summer.

Seasonal temperature variations (Figs. 5E–H) also vary between the different time slices and regions. The summer–winter temperature amplitude is higher during the LGM and MH (18–25 °C) than in the PI (14–16 °C). For example, in the southern regions the winter–summer temperature difference is ~20 °C for the LGM, ~18 °C for the MH and ~14 °C for the PI (Fig. 5E). Furthermore, the LGM and MH temperature anomalies (relative to the PI) also show more pronounced seasonal variation. The LGM is colder (8.0–10 °C) in winter but LGM summer temperature is about the same as during the PI times. MH temperature is higher (2.0–7.0 °C) in summer but colder (3.0–5.0 °C) in winter than during the PI times. The western region is characterized by the largest MH temperature differences, i.e. a summer warming of 7.0 °C and winter cooling of 5.0 °C (Fig. 5G).

Seasonal precipitation variations (Figs. 5I–L) demonstrate that: first, a strong influence of the monsoon in the southern and eastern regions for the LGM and MH simulations. For example, the southern region LGM precipitation increases from 18.1 mm/month in the winter to 288 mm/month in the summer (Fig. 5I). In the eastern region, precipitation increases from 6.5 mm/month in the winter to 180 mm/month in summer (Fig. 5L). Second, the LGM and MH precipitation anomalies also show different regional and seasonal variation. The LGM winter is drier than the PI winter across the Tibetan Plateau except in the south region. For example, LGM winter precipitation is 6.0 mm/month higher than during PI times (18.1 vs 12.1 mm/month) (Fig. 5I). LGM summers are wetter in the southern (LGM: 288 mm/month, PI: 243 mm/month) and northern regions (LGM: 58.8 mm/month, PI: 28.0 mm/month)

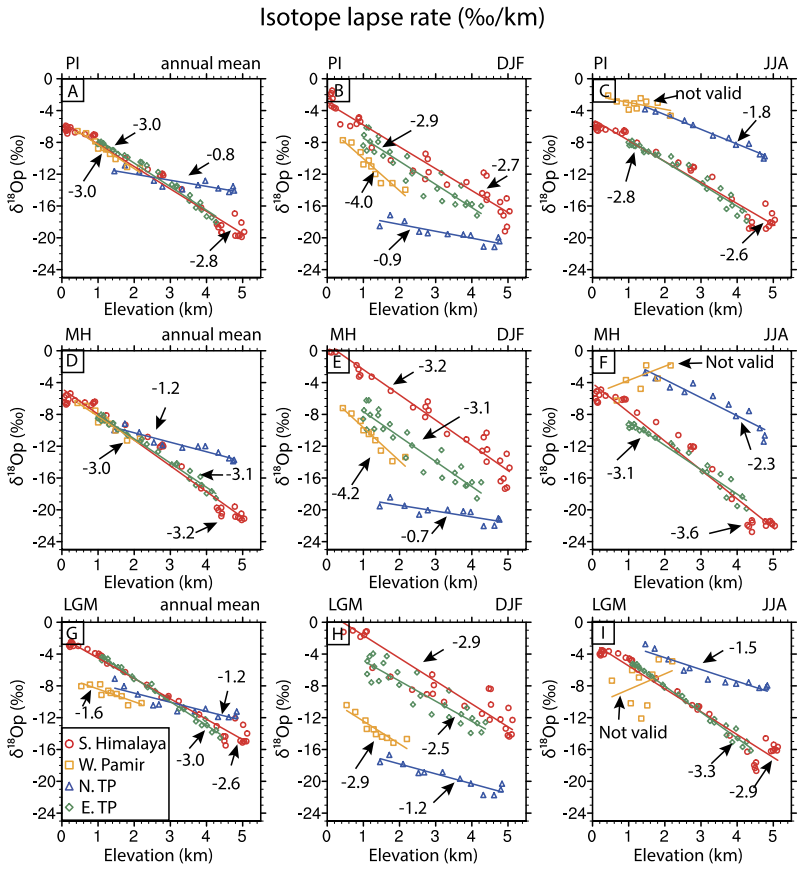

Fig. 6. Model simulated isotope lapse rate during the PI (top row), MH (middle row) and LGM (bottom row). The analysis has been conducted at 4 mountain slopes: the south slope of the Himalaya (25°N–30°N, 84°E–92°E) (red cycle), west slope of the Pamir (36°N–38°N, 65°E–70°E) (orange square), north slope of the Tibetan Plateau (36°N–39°N, 85°E–89°E) (blue triangle) and the east slope of the Tibetan Plateau (32°N–36°N, 100°E–110°E) (green diamond). The precipitation weighted temporal differences are presented for the annual mean (left column), winter season (DJF) (middle column) and monsoon season (JJA) (right column). The uncertainty of slopes and their significant level are listed in Table S3 in the supplementary material. (For interpretation of the references to color in this figure legend, the reader is referred to the web version of this article.)

(Figs. 5I and J). MH summer precipitation is lower than the PI precipitation in the western region (MH: 28.4 mm/month, vs PI: 59.0 mm/month), and MH winter precipitation is 22.3 mm/month but PI precipitation is 25.5 mm/month (Fig. 5K).

Taken together, the above results suggest: (1) LGM and MH both have higher seasonal (winter–summer) amplitudes in $\delta^{18}O_p$, temperature and precipitation values than during PI times. Of the four regions analyzed, these seasonal differences are most pronounced in the western region. (2) Based on the climatological mean anomalies discussed in the previous section, the LGM is generally colder and drier and the MH is colder and wetter than the PI climate. (3) The three $\delta^{18}O_p$ distributions zones observed in the modern (Yao et al., 2013) also existed during the MH and LGM as well.

3.3. Spatial and temporal variations in isotope lapse rates during the PI, MH and LGM

In this study, spatial and temporal variations of the model simulated isotopic lapse rate have been analyzed at four high relief zones on the flanks of the plateau (red boxes in Fig. 4). The locations include the southern slope of the Himalaya (25°N–30°N, 84°E–92°E), western slope of the Pamir (36°N–38°N, 65°E–70°E), northern slope of the Tibetan Plateau (36°N–39°N, 85°E–89°E), and the eastern slope of the Tibetan Plateau (32°N–36°N, 100°E–110°E). The analysis has been done for the winter season (DJF), monsoon season (JJA), and precipitation weighted annual mean (Fig. 6). The statistical analysis of the estimated isotopic lapse rates including uncertainty and the significant level is shown in Table S3 in supplementary material.

Significant temporal changes in the isotopic lapse rate are evident from the model results (Fig. 6). The primary trends in the model results include: (1) some regional variations in the mean annual and seasonal isotope lapse rates. For example, the southern Himalayan front has a similar lapse rate (~3.0‰/km) as the eastern Tibetan Plateau (red lines overlay or are parallel to the green lines), but the northern slope of the Plateau (blue lines) has a lower isotope lapse rate than the slopes in the southern and eastern regions (e.g. Figs. 6A, C, D, G, I). The western Pamir region has a higher isotope lapse rate in the winter than the other regions (Figs. 6B, E, H). For example, the MH winter west Pamir lapse rate is −4.2‰/km, whereas the southern and eastern lapse rates are ~−3.2‰/km and the northern lapse rate is −0.7‰/km (Fig. 6E). (2) Different regions have different seasonal variation in the isotope lapse rate. The southern and eastern slopes have the lowest seasonal variation (~0.2‰/km, max 0.4‰/km) (compare Figs. 6B, E, H with Figs. 6C, F, I). The summer isotope lapse rate calculated for the west slope of the Tibetan Plateau (Figs. 6C, F, I) are not significant at the 95% significance level, which is due to model limitations for calculating lapse rate when precipitation rates are very low. Finally, (3) the precipitation weighted annual mean isotope lapse rates in the three time slices (PI, MH and LGM) indicate the smallest differences in the lapse rate (~0.1‰/km) occur on the eastern slope between each time slice. The largest difference (~1.4‰/km) is found in the western slope where the largest uncertainty is (Table S3). The northern slope has a mean annual

difference of ~0.4‰/km between the LGM, MH and PI whereas for the southern slope, the isotope lapse rate is about 0.4‰/km larger during the MH and 0.2‰/km smaller during the LGM than during the PI (Figs. 6A, D and G).

4. Discussion

4.1. Comparisons between the simulated anomalies and the proxy-based reconstructions during the MH and LGM

The simulated anomalies have been compared with climate change reconstructions based on proxy data (see supplemental Tables S1, S2 for data used). In most cases climate reconstructions from proxy data indicate a change relative to a known condition, such as the PI times, and do not provide an absolute value or magnitude of the changes. As a result, the changes can only be described here in relative terms, i.e. as 'wetter than', 'similar to' and 'drier than' for precipitation, and 'warmer than', 'similar to' and 'colder than' for temperature. The PI climate serves as our reference climate for these descriptions. The proxy data based changes are plotted over the model simulated precipitation and temperature anomalies for the MH (Fig. 7A) and LGM (Figs. 7B and C).

There is both an agreement and disagreement between the model and observations during the MH (Fig. 7A). Model and observations agree at the Himalayan front that the MH climate is wetter than the PI climate. On the northeast part of the Tibetan Plateau, MH proxy data show a large disagreement between neighboring locations, e.g. at locations 2–6, 9–10, 12, 18–19, 22–23 and 25 in Fig. 7A, whereas the model shows no significant change at the 95% confidence level (represented by the white color in Fig. 7A). The model results from GCMs suggest that the climate change in this region is muted and the variations in the proxy data might result from different methods (Table S1) and localized climate signals. The above results agree with previous work (Dallmeyer et al., 2013) that conducted a similar comparison between the MH and PI climates. Their results show a wetter MH climate at the south and middle Tibetan Plateau, and suggested a regional dissimilarity in the annual precipitation signal between the MH and PI climate as well.

There is better agreement between model and observations for the LGM than for the MH (Figs. 7B and C). Predicted temperature changes show good agreement with the proxy data in both the sign and magnitude of the predicted change (Fig. 7B). Schmidt et al. (2011) derived an LGM max ΔT of 3.0 to 4.0 °C from biogeographical and phylogenetic data of biomarkers at location 6 in Fig. 8A where the model simulated LGM temperature difference is −3.7 °C. Herzschuh et al. (2006) derived a ~4.0–7.0 °C colder temperature during the LGM from the vegetation of a sediment core at the Qilian Mountains where the model simulated result is −4.7 °C. The predicted precipitation differences also show a good agreement with the proxy data (Fig. 7C). The sign of the simulated LGM precipitation changes agrees with the existing proxy data near the Himalaya (locations 2, 3 in Fig. 7C), at the Zabuye salt lake on the central Tibetan Plateau (location 5), at Qilian Mt (location 7), and at Xinyun lake in the South China (locations 9, 10). Model predictions also indicate both wetter, drier, and similar to present LGM precipitation condition for the central Himalaya (red, blue, and white colors in Fig. 7C), and one proxy studies in this region (location 1) suggest precipitation conditions the same as today (Asahi, 2010).

Unfortunately, a more detailed comparison between GCM predictions and proxy data cannot be completed. This is mainly due to the fact that many of the available proxy data indicate only a relative change in conditions, such that other parameters like changes in the maximum and minimum predicted and observed temperature or precipitation cannot be compared. No better or worse

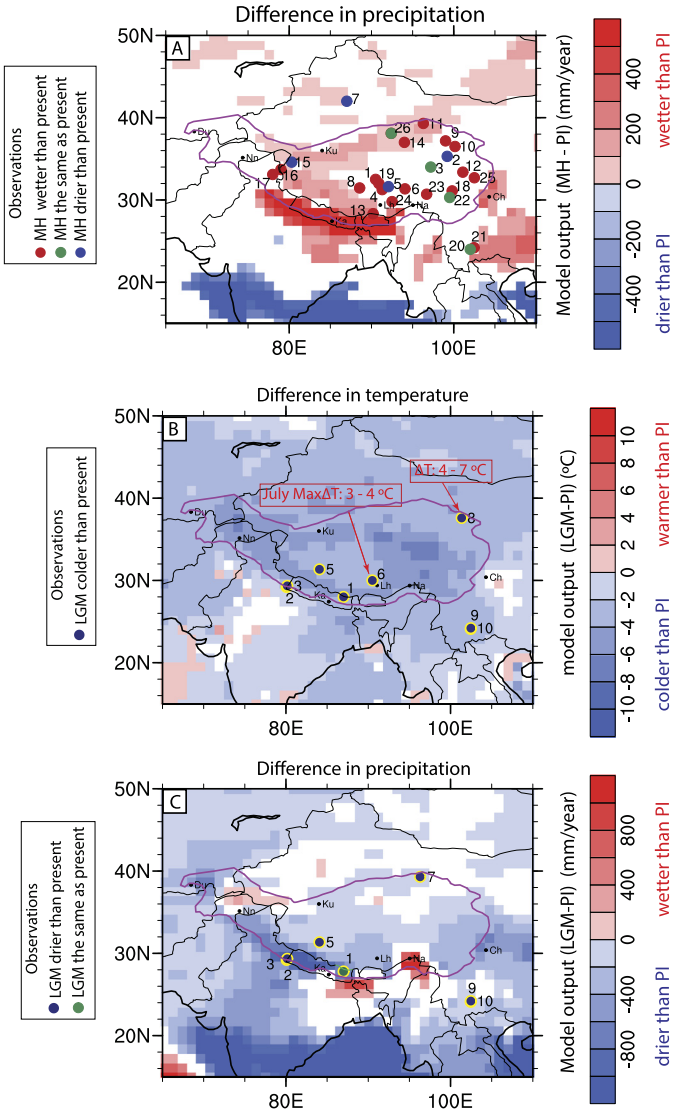

Fig. 7. (A) MH model and proxy data comparison. Locations and references cited on the plot: 1. Nam co, Muegler et al. (2010). 2. Lake Kuhai, Wischnewski et al. (2011). 3. Lake Koucha, Mischke et al. (2008). 4. Lake Cuoe, Wu et al. (2006). 5. Ahung co, Morrill et al. (2006). 6. Lake Zabuye Salt, Wang et al. (2002). 7. Kaidu River, Wuennemann et al. (2006). 8. Selin Co, Zhang et al. (2011). 9. Lake Qinghai, Shen et al. (2005). 10. Lake Qinghai, Liu et al. (2014). 11. Mt. Qilian, Herzschuh et al. (2005). 12. Lake Ximencuo, Zhang and Mischke (2009). 13. Pumoyum Co, Nishimura et al. (2014). 14. Qaidam Basin, Yu and Lai (2014). 15. Sumxi Co, Gasse et al. (1991). 16. Lake Bangong, Van Campo et al. (1996). 17. Lake TsoKar, Demske et al. (2009). 18. Lake Naleng, Kramer et al. (2010), Wischnewski et al. (2011). 19. Lake Zigetang, Herzschuh et al. (2006). 20. Lake Qiliu, Hodell et al. (1999), Zhang et al. (2011). 21. Lake XingYun, Hodell et al. (1999), Zhang et al. (2011). 22. Lake Yidun, Shen et al. (2006), Wischnewski et al. (2011). 23. Ren Co, Tang et al. (2000). 24. Lake Hidden, Tang et al. (2000). 25. Hongyun, Zhou et al. (2002), Wischnewski et al. (2011). 26. Dunde Ice Core, Liu et al. (1998), Wischnewski et al. (2011). LGM temperature (B) and precipitation (C) model and proxy data comparison. Locations and references cited on the plot: 1. Eastern Nepal Himalaya, Asahi (2010). 2. Kumaun Himalaya, Kotlia et al. (2010). 3. Kumaun Himalaya, Kotlia et al. (2000). 5. Zabuye Salt lake, Wang et al. (2002). 6. Yarlung Zhangbo catchment, Schmidt et al. (2011). 7. West Qilian Mt., Hu et al. (2014). 8. Qilian Mt., Herzschuh et al. (2006). 9. 10. Xinyun Lake, Hodell et al. (1999). (For interpretation of the references to color in this figure legend, the reader is referred to the web version of this article.)

agreement between certain types of proxy data and the GCM results can be determined with the available data. Agreement and disagreement can be seen among the same type of proxy data with the GCM results for the MH (Table S1). We note however that the agreement between the model and data for the LGM is generally good, despite the fact that the eight LGM proxy studies used in-

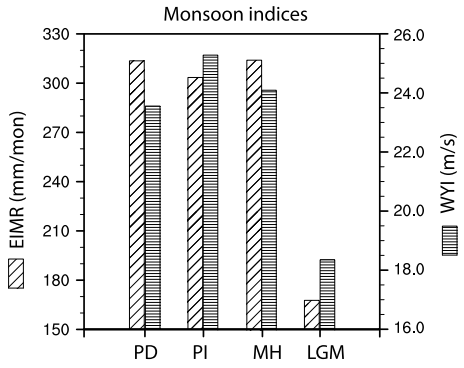

Fig. 8. EIMR (Goswami et al., 1999) and WYI (Webster and Yang, 1992) monsoon index calculated from the simulated long-term mean data during the PD, PI, MH and LGM. The mean and standard derivation of simulated yearly EIMR and WYI are listed in Table S4 in supplement material.

cluded six different proxy methods (Table S2). From our analysis we can however conclude that: (1) MH climate change relative to today is muted and the climate anomalies might lie in the uncertainty of both predicted GCM values and proxy data. Finally, (2) paleo climate change for the LGM is consistently reconstructed by both the GCM and proxy studies.

4.2. Length and intensity of Indian monsoon during the PI, MH and LGM

Precipitation over the Tibetan Plateau is strongly influenced by the Indian monsoon. The intensity and the period of the monsoon system can be identified with various methods. In this study, we used the Extended Indian Monsoon rainfall index (EIMR) and Wesbter and Yang Index (WYI) to identify the variations of the monsoon intensity during the MH and LGM (Fig. 8). The EMIR is defined as the summer (JJAS) rainfall in the continental region between 70°E–110°E and 10°N–30°N (Goswami et al., 1999). WYI is defined as the difference in zonal wind speed at 850 hPa and 200 hPa for the region 40°E–110°E and 0°–20°N (Webster and Yang, 1992). Using the GCM predicted wind field and a bulk trajectory analysis method, the source of the vapor and the length of the monsoon period during the LGM, MH and PI are determined in this study (Fig. 9). The bulk trajectory analysis is the backtracking of the moisture only in the boundary layer (1000 to 850 hPa) where the vapor is concentrated (Feng et al., 2013).

Both the EIMR and WYI monsoon index suggest significantly reduced monsoon intensity during the LGM (Fig. 8). Relative to the PI climate, the LGM had a 44.5% decrease in EIMR (decreased from 304 mm/month during the PI to 168 mm/month during the LGM), and a 27.6% decrease in WYI (decrease from 25.4 m/s during the PI to the 18.4 m/s during the LGM) in comparison to PI conditions. The changes of the MH monsoon intensity relative to the PI are not consistent between both calculation methods but those changes are minor (Fig. 8). For example, the EIMR increases from 303 mm/month during PI to 314 mm/month during the MH (~3.6% increase), while the WYI decreases from 25.4 m/s during the PI to 24.2 m/s during the MH (~4.7% decrease). The standard deviation (σ) of EIMR and WYI for the simulation years is summarized in Table S4. The σ of EIMR ranges from 8.4–19 mm/month, and the σ of WYI ranges from 0.8–2.1 m/s.

The inter-annual bulk trajectory analysis shows that the length of the LGM monsoon is about one month shorter than during the PI, and that there are no obvious differences in the monsoon length between the MH and PI (Fig. 9). During the winter (NDJFMA) (Figs. 9A, F and K show an example for January), the dominantly westerly winds demonstrate that no monsoon exits during this time. The onset of the monsoon is marked by the beginning of the moisture originating from the Indian Ocean, which happens in May for all three time slices (Figs. 9B, G and L). The decline of the monsoon initiated in October during the PI (Fig. 9E) and the MH (Fig. 9J), but occurs a month earlier, in September, during the LGM (Fig. 9N).

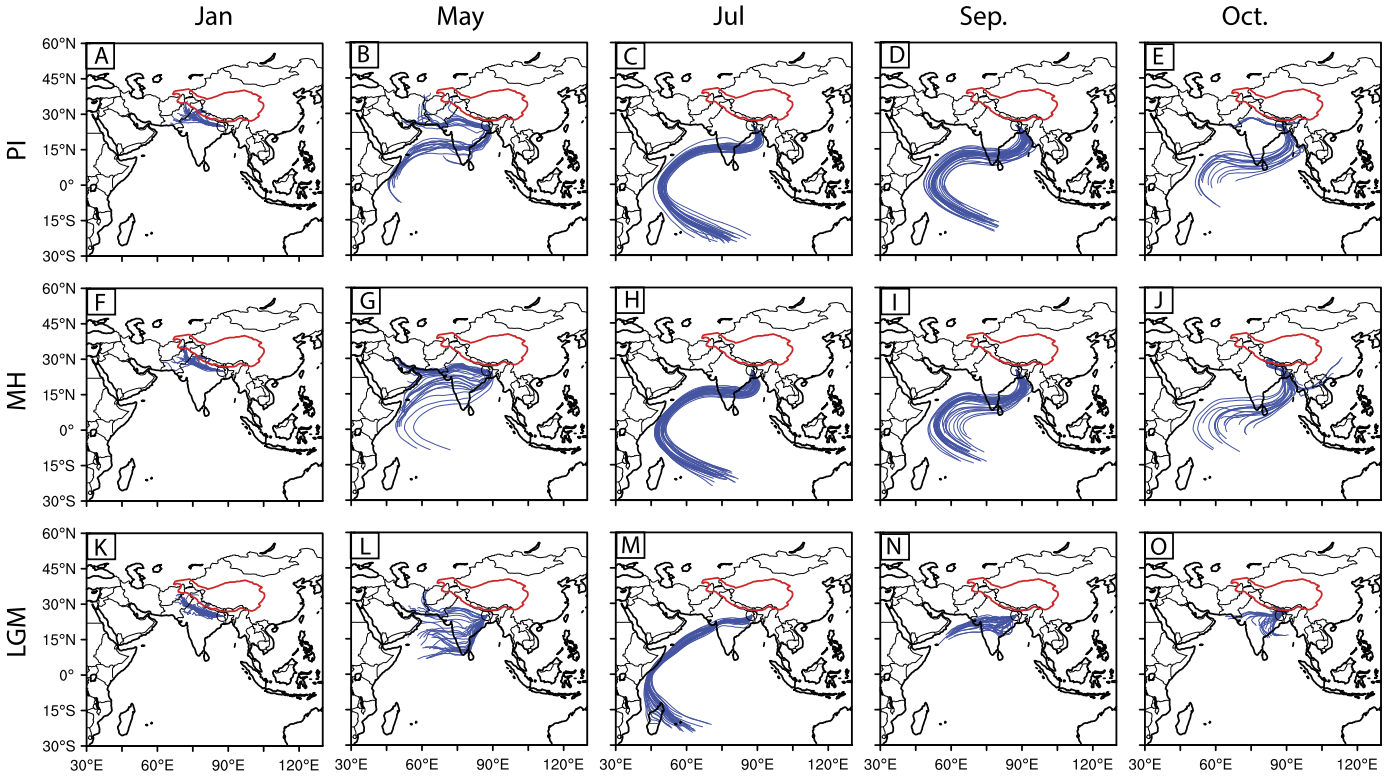

Fig. 9. Interannual bulk trajectory analysis at 25°N, 87.5°E. It tracks the bulk moisture in the boundary layer (1000 to 850 hPa) where the vapor is concentrated (Feng et al., 2013). The location lies at the south of the Himalayan front, which is a potential vapor source of precipitation on the Tibetan Plateau during the monsoon season.

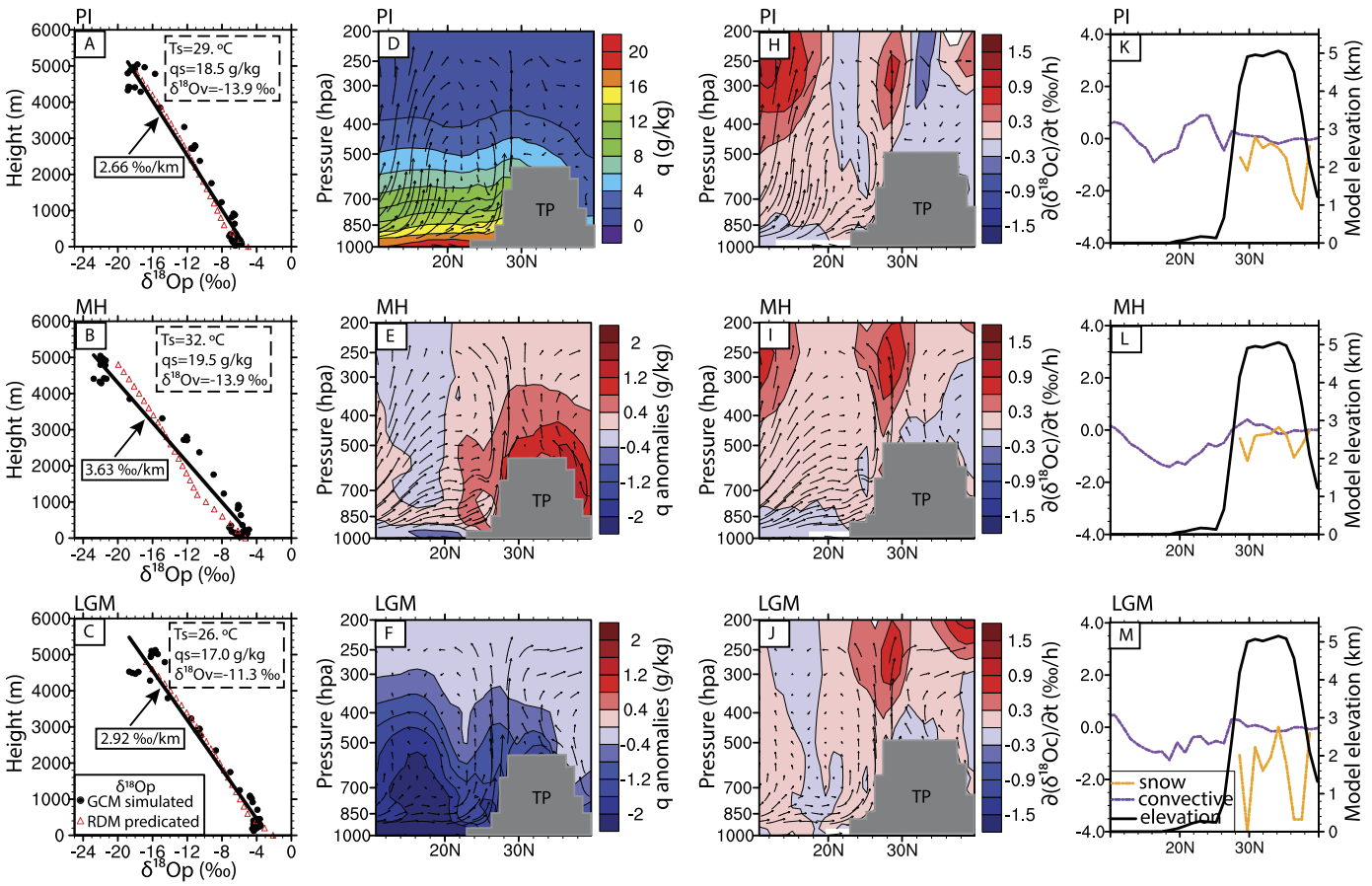

Fig. 10. RDM and GCM comparison and related atmospheric processes for the monsoon season (JJA) during the PI, MH and LGM at Himalaya front (zonal average between 84°E–92°E). (A–C) RDM and GCM $\delta^{18}O_p$ comparison. Model $\delta^{18}O_p$ are presented as solid dots and black solid line (trend line from a linear fitting). The red triangle represents the RDM estimation initiated with GCM derived moisture source. The initial vapor source are presented as three variables: T_s, q_s and $\delta^{18}O_v$ (listed in the dash box), where T_s is the initial vapor temperature, q_s is the initial vapor specific humidity and $\delta^{18}O_v$ is the $\delta^{18}O$ in the initial water vapor. (D–F) Model simulated specific humidity at cross section 10°N–40°N. Colors contour represent q or q anomaly values. Streamlines represent the vertical wind (omega) and the meridional wind (v) field. The Tibetan Plateau is shaded in gray. (H–J) Estimated $\delta^{18}O_v$ mixing rate at cross section 10°N–40°N, data are zonally averaged between 84°E–92°E during JJA. The mixing rate is defined as the change of $\delta^{18}O_p$ due to the mixing effect of water vapor with its environment (units: ‰/h). Streamlines represent vertical wind (omega) and meridional wind (v) field. The Tibetan Plateau is shaded in gray. (K–M) Changes in $\delta^{18}O_p$ if one precipitation type is absent. Purple represents the changes in $\delta^{18}O_p$ if the convective precipitation is absent, orange represents changes in $\delta^{18}O_p$ if the snow type is absent. The elevation of the Tibetan Plateau is plotted as black solid line. (For interpretation of the references to color in this figure legend, the reader is referred to the web version of this article.)

4.3. Correlations between temperature and precipitation with $\delta^{18}O_p$

Temperature, topography and precipitation are the most important climate controls on $\delta^{18}O_p$. In this study, we correlate model-predicted $\delta^{18}O_p$ with temperature and precipitation, and correlate temperature with precipitation (Fig. S1). The seasonal cycle has been removed from the model output to filter out the seasonal signal in the analysis (to avoid high correlation coefficients produced by season-dependent co-variability of the investigated variables). The correlation analyses are conducted for each grid box with a population of more than 120 data points. Only the correlation coefficients that are above the 95% significance level are shown in the plot (Fig. S1). The correlation analyses indicates (1) a significant positive correlation of $\delta^{18}O_p$ and temperature in the region $>\sim$30°N, and a negative correlation between $\delta^{18}O_p$ and precipitation in the region <40°N. (2) The dominant control of temperature on $\delta^{18}O_p$ at the high altitudes and precipitation on $\delta^{18}O_p$ at low altitudes may be explained by an overshadowing of the effect of temperature in latitudes governed by higher precipitation rates (the South). (3) On the Tibetan Plateau, the temperature control is insignificant, possibly because the variability in temperature that is relevant to $\delta^{18}O_p$ variability lies mostly in the seasonal cycle which has been removed. (4) The pattern of correlation coefficients does not vary much between the different time slices, suggesting that the different climates during the LGM, MH and PI have little or no influence on the spatial dependence of the control of temperature and precipitation on $\delta^{18}O_p$ in this region.

4.4. GCM and RDM approaches for estimating $\delta^{18}O_p$ during the PI, MH and LGM

The comparison between the more simple one-dimensional RDM and more comprehensive GCM predicted $\delta^{18}O_p$ was conducted on the south slope of the Himalaya (84°E–92°E, 23°N–30°N) during the monsoon season JJA. The initial vapor moisture conditions (represented as T_s, q_s and $\delta^{18}O_v$) used for the RDM calculation are derived from the GCM output, where T_s is the initial vapor temperature, q_s is the initial vapor specific humidity and $\delta^{18}O_v$ is the $\delta^{18}O$ in the initial water vapor.

Results show that the RDM agrees with the GCM during the PI (Fig. 10A) and LGM times (Fig. 10C). During the MH, the RDM predicts more depleted $\delta^{18}O_p$ at ~1 km elevation and ~2.0‰ more enriched $\delta^{18}O_p$ than the GCM prediction at ~5 km elevation (Fig. 10B). The differences in the RDM and GCM predictions during the MH can be explained in part by warmer conditions and more vapor content in the initial moisture source during the MH than that during the PI for the RDM calculations (dash boxes in Figs. 10A and B, and Figs. 10D and E).

Various climate processes that the RDM does not consider include mass mixing, vapor recycling, changes in the wind field and vapor sources, and changes in the precipitation type (Feng et al., 2013). The mass mixing is the mixing of the air parcel with its environment that results in a change in $\delta^{18}O_p$. The vapor recycling represents the ratio of recycling water vapor into the air parcel due to the re-evaporation. The changes in the precipitation type describe the changes in $\delta^{18}O_p$ if certain precipitation is not present. In the North American Cordillera, those processes had significant (>2.0‰) influence on the $\delta^{18}O_p$ (Feng et al., 2013). Among those processes, three of them are suggested by us to have little or no influence on the $\delta^{18}O_p$ for the Tibetan Plateau region. The mixing ratio is not significant (<0.2‰/h) (Figs. 10H, I, J) in comparison with the 3.0‰/h at the North American Cordillera. The influence of vapor recycling can be neglected due to the low recycling factor (defined as the ratio of evaporation and precipitation) (~10–20%) at the Himalayan front) (Fig. S2). The wind field and vapor sources stay the same during the PI, MH and LGM (Fig. 9). For the changes in precipitation type, snowfall can reduce the $\delta^{18}O_p$ up to 4.0‰ during the LGM, up to 1.0‰ during the MH, and the convective precipitation can change up to 1.0‰$\delta^{18}O_p$ (Figs. 10K, L and M). The processes that can compensate the influence of precipitation type change on $\delta^{18}O_p$ during the LGM, and the processes that cause the RDM and GCM differences shown are not completely known, and need further investigation. The comparison of the RDM and GCM approaches suggest that the simpler RDM approach captures most of the fractionation processes (except the precipitation type change) for the Himalayan front, as long as the $\delta^{18}O_p$ of low elevation locations is known for the past times slices.

5. Summary

In this study, variations in climate and $\delta^{18}O_p$ during the LGM and MH were compared to PI times using a GCM with an isotope model (ECHAM5-wiso). Five primary conclusions were reached by this study.

1. Results show muted climate change across the plateau during the MH, and larger changes occurring during the LGM. During the LGM surface temperatures are ~2.0–4.0 °C lower across the Himalaya and Tibet, >5.0 °C lower at the northwest and northeast edge of the Tibetan Plateau. Mean annual precipitation is 0.2–0.6 m/yr lower over on the Tibetan Plateau and LGM $\delta^{18}O_p$ is 2.0–4.0‰ enriched relative to pre-industrial estimates.

2. Model and proxy data comparisons show a good agreement for the LGM and large differences for the MH, but those disagreements exist even within the MH proxy data themself. This results suggested that the MH climate change anomalies are too small to reliably reconstruct from either the GCM or proxy studies. In contrast, a climate change signal for the LGM is well resolved by both the GCM and proxy methods.

3. Isotope lapse rates on the high relief flanks of the Tibetan Plateau vary spatially and temporally. The precipitation weighted annual mean isotope lapse rate at the Himalaya front is about 0.4‰/km larger during the MH and 0.2‰/km smaller during the LGM than that during the PI. The correlations analyses using temperature, precipitation and $\delta^{18}O_p$ show a north–south pattern (significant positive correlation of $\delta^{18}O_p$ and temperature in the region >~30°N, and a negative correlation between $\delta^{18}O_p$ and precipitation in the region <40°N). The pattern of correlation coefficients does not vary much among the PI, MH and LGM, which suggest that the different Quaternary climates have little or no influence on the spatial dependence of the control of temperature and precipitation on $\delta^{18}O_p$ in this region.

4. The length and intensity of the Indian monsoon during the MH and PI are similar. The rainfall associated with the Indian monsoon is about 44% less in the LGM than during PI times. The LGM monsoon period is about one month shorter than that in PI times. The onset of the monsoon during the LGM, MH and PI is similar, but the decline of the monsoon initiated in September during the LGM instead of October as during the PI and MH.

5. Finally, our comparison between a commonly used 1D Rayleigh Distillation Model (RDM) and the GCM $\delta^{18}O_p$ suggest that the influence of vapor mixing, changes in the wind direction and vapor sources, and re-cycling of evaporated vapor are not significant. The change of precipitation type to snow during the LGM can cause up to 4‰ changes in $\delta^{18}O_p$ that could influence some proxy data.

Acknowledgements

This project (DFG-EH329/2-1) is found by the German Research Foundation (DFG) and is part of the TIP SPP program 1372 (Tibetan Plateau: Formation, Climate, Ecosystems). The authors would also like to acknowledge the role of the Deutsches Klimarechenzentrum (DKRZ) in granting necessary computing resources required for this study. The data are available from the authors upon request (todd.ehlers@uni-tuebingen.de). Chris Poulsen and Ran Feng are thanked for their input on the development of the RDM model used in this study.

Appendix A. Supplementary material

Supplementary material related to this article can be found online at http://dx.doi.org/10.1016/j.epsl.2016.09.031.

References

Arnold, L., Breon, F.M., Brewer, S., 2009. The earth as an extrasolar planet: the vegetation spectral signature today and during the last Quaternary climatic extrema. Int. J. Astrobiol. 8, 81–94. http://dx.doi.org/10.1017/S1473550409004406.

Asahi, K., 2010. Equilibrium-line altitudes of the present and Last Glacial Maximum in the eastern Nepal Himalayas and their implications for SW monsoon climate. Quat. Int. 212, 26–34.

Braconnot, P., Otto-Bliesner, B., Harrion, S., Joussaume, S., Peterschmitt, J.-Y., Abe-Ouchi, A., Crucifix, M., Driesschaert, E., Fichelfet, Th., Hewitt, C.D., Kagayama, M., Kitoh, A., Laine, A., Loutre, M.-F., Marti, O., Merkel, U., Ramstein, G., Valdes, P., Weber, S.L., Yu, Y., Zhao, Y., 2007. Results of PMIP2 coupled simulations of the Mid-Holocene and Last Glacial Maximum – part 1: experiments and large-scale feature. Clim. Past 3, 261–277.

Chamberlain, C.P., Poage, M.A., 2000. Reconstructing the paleo-topography of mountain belts from the isotopic composition of authigenic minerals. Geology 28, 115–118.

Dallmeyer, A., Claussen, M., 2011. The influence of land cover change in the Asian monsoon region on present-day and mid-Holocene climate. Biogeosciences 8, 1499–1519. http://dx.doi.org/10.5194/bg-8-1499-2011.

Dallmeyer, A., Claussen, M., Wang, Y., Herzschuh, U., 2013. Spatial variability of Holocene changes in the annual precipitation pattern: a model-data synthesis for the Asian monsoon region. Clim. Dyn. 40, 2919–2936. http://dx.doi.org/10.1007/s00382-012-1550-6.

Demske, D., Tarasov, P.E., Wuennemannand, B., Riedel, F., 2009. Late glacial and Holocene vegetation, Indian monsoon and westerly circulation in the Trans-Himalaya recorded in the lacustrine pollen sequence from Tso Kar, Ladakh, NW India. Palaeogeogr. Palaeoclimatol. Palaeoecol. 279, 172–185.

Dietrich, S., Werner, M., Spangehl, T., Lohmann, G., 2013. Influence of orbital forcing and solar activity on water isotopes in precipitation during the mid- and late Holocene. Clim. Past 9, 13–26.

Ehlers, A.T., Poulsen, C.J., 2009. Influence of Andean uplift on climate and paleoaltimetry estimates. Earth Planet. Sci. Lett. 281 (3–4), 238–248.

Feng, R., Poulsen, C.J., Werner, M., Chamberlain, C.P., Mix, H.T., Mulch, A., 2013. Early Cenozoic evolution of topography, climate, and stable isotopes in precipitation in the north American cordillera. Am. J. Sci. 313, 613–648. http://dx.doi.org/10.2475/07.3013.01.

Gasse, F., Arnold, M., Fontes, J.C., Fort, M., Gibert, E., Huc, A., Li, B., Li, Y., Liu, Q., Melleres, F., Van Campo, E., Wang, F., Zhang, Q., 1991. A 13,000-year climate record from western Tibet. Nature 353, 742–745.

Goswami, B.N., Krishnamurthy, V., Annamalai, H., 1999. A broad-scale circulation index for the interannual variability of the Indian summer monsoon. Q. J. R. Meteorol. Soc. 125, 611–633.

Graham, S.A., Chamberlain, C.P., Yue, Y.J., Ritts, B.D., Hanson, A.D., Horton, T.W., Waldbauer, J.R., Poage, M.A., Feng, X., 2005. Stable isotope records of Cenozoic climate and topography, Tibetan plateau and Tarim basin. Am. J. Sci. 305 (2), 101–118.

Herschuh, U., Zhang, C., Mischke, S., Herzschuh, R., Mohammadi, F., Mingram, B., Kuerschner, H., Riedel, F., 2005. A late quaternary lake record from the Qilian Mountains (NW China): evolution of the primary production and the water depth reconstructed from marofossil, pollen, biomarker, and isotope data. Glob. Planet. Change 46, 361–379.

Herzschuh, U., Kuerschner, H., Mischke, S., 2006. Temperature variability and vertical vegetation belt shifts during the last ~50,000 yr in the Qilian Mountains (NE margin of the Tibetan Plateau China). Quat. Res. 66, 133–146.

Hodell, D.A., Brenner, M., Kanfoush, S.L., Curtis, J.H., stoner, J.S., Song, X., Wu, Y., Whitmore, T.J., 1999. Paleoclimate of southwestern China for the past 50,000 yr inferred from lake sediment records. Quat. Res. 52, 369–380.

Hren, M.T., Bookhagen, B., Blisniuk, P.M., Booth, A.L., Chamberlain, C.P., 2009. $\delta^{18}O$ and δD of streamwaters across the Himalaya and Tibetan Plateau: implications for moisture sources and paleoelevation reconstructions. Earth Planet. Sci. Lett. 288, 20–32.

Hu, G., Yi, C.-L., Zhang, J.-F., Liu, J.-L., Jiang, T., Qin, X., 2014. Optically stimulated luminescence dating of a moraine and a terrace in Laohugou valley, western Qilian Shan, northeastern Tibet. Quat. Int. 321, 37–49.

Kent-Corson, M.L., Ritts, B.D., Zhuang, G.S., Bovet, P.M., Graham, S.A., Chamberlain, C.P., 2009. Stable isotopic constraints on the tectonic, topographie, and climatic evolution of the northern margin of the Tibetan Plateau. Earth Planet. Sci. Lett. 282 (1–4), 158–166.

Kotlia, B.S., Sharma, C., Bhalla, M.S., Rajagopalan, G., Subrahmanyam, K., Bhattacharyya, A., Valdiya, K.S., 2000. Paleoclimatic conditions in the late Pleistocene Wadda Lake, eastern Kumaun Himalaya (India). Palaeogeogr. Palaeoclimatol. Palaeoecol. 162, 105–118.

Kotlia, B.S., Sanwal, J., Phartiyal, B., Joshi, L.M., Trivedi, A., Sharma, C., 2010. Late Quaternary climatic changes in the eastern Kumaun Himalaya, India, as deduced from multi-proxy studies. Quat. Int. 213, 44–55.

Kramer, A., Herzschuh, U., Mischke, S., Zhang, C., 2010. Late glacial vegetation and climate oscillations on the southeastern Tibetan Plateau inferred from the lake Naleng pollen profile. Quat. Res. 73, 324–335.

Langebroek, P.M., Werner, M., Lohmann, G., 2011. Climate information imprinted in oxygen-isotopic composition of precipitation in Europe. Earth Planet. Sci. Lett. 311, 144–154.

Liu, K., Yao, Z., Thompson, L.G., 1998. A pollen record of Holocene climatic changes from the Dunde ice cap, Qinghai-Tibetan Plateau. Geology 26, 135–138.

Liu, X., Colman, S.M., Brown, E.T., An, Z., Zhou, W., Timothy Jull, A.J., Huang, Y., Cheng, P., Liu, W., Xu, H., 2014. A climate threshold at the eastern edge of the Tibetan plateau. Geophys. Res. Lett. http://dx.doi.org/10.1002/2014GL060833.

Lorenz, S.J., Lohmann, G., 2004. Acceleration technique for Milankovitch type forcing in a coupled atmosphere–ocean circulation model: method and application for the Holocene. Clim. Dyn. 23, 727–743. http://dx.doi.org/10.1007/s00382-004-0469-y.

Mischke, S., Kramer, M., Zhang, C., Shang, H., Herschuh, U., Erzinger, J., 2008. Reduced early Holocene moisture availability in the Bayan Har Mountains, northeastern Tibetan Plateau, inferred from a multi-proxy lake record. Palaeogeogr. Palaeoclimatol. Palaeoecol. 267, 59–76.

Morrill, C., Overpeck, J.T., Cole, J.E., Liu, K.-B., Shen, C., Tang, L., 2006. Holocene variations in the Asian monsoon inferred from the geochemistry of lake sediments in central Tibet. Quat. Res. 65, 232–243.

Muegler, I., Gleixner, G., Guenther, F., Maeusbacher, R., Daut, G., Schuett, B., Berking, J., Schwalb, A., Schwark, L., Xu, B., Yao, T., Zhu, L., Yi, C., 2010. A multi-proxy approach to reconstruct hydrological changes and Holocene climate development of Nam Co, Central Tibet. J. Paleolimnol. 43, 625–648. http://dx.doi.org/10.1007/s10933-009-9357-0.

Nishimura, M., Matsunaka, T., Morita, Y., Watanabe, T., Nakamura, T., Zhu, L., Nara, F.W., Imai, A., Izutsu, Y., Hasuike, K., 2014. Paleoclimatic changes on the southern Tibetan Plateau over the past 19,000 years recorded in lake Pumoyum Co, and their implications for the southwest monsoon evolution. Palaeogeogr. Palaeoclimatol. Palaeoecol. 396, 75–92.

Otto-Bliesner, B.L., Brady, E.C., Glauzet, G., Tomas, R., Levis, S., Kothavala, Z., 2006. Last glacial maximum and Holocene climate in CCSM3. J. Climate 19, 2526–2544.

Rowley, D.B., Garzione, C.N., 2007. Stable isotope-based paleoaltimetry. Annu. Rev. Earth Planet. Sci. 35, 463–508.

Schmidt, J., Opgenoorth, L., Martens, J., Miehe, G., 2011. Neoendemic ground beetles and private tree haplotypes: two independent proxies attest a moderate last glacial maximum summer temperature degression of 3–4 °C for the southern Tibetan Plateau. Quat. Sci. Rev. 30, 1918–1925.

Shen, J., Liu, X.Q., Wang, S.M., Matsumoto, R., 2005. Palaeoclimatic changes in the Qinghai, Lake area during the last 18,000 years. Quat. Int. 136, 131–140.

Shen, C., Liu, K., Tang, L., Overpeck, J.T., 2006. Quantitative relationships between modern pollen rain and climate in the Tibetan Plateau. Rev. Palaeobot. Palynol. 140, 61–77.

Tang, L., Shen, C., Liu, K., 2000. Changes in south Asian monsoon: new high-resolution paleoclimatic records from Tibet, China. Chin. Sci. Bull., 87–91.

Tian, L.D., Yao, T.D., MacClune, K., White, J.W.C., Schilla, A., Vaughn, B., Vachon, R., Ichiyanagi, K., 2007. Stable isotopic variations in west China: a consideration of moisture sources. J. Geophys. Res., Atmos. 112, D10112.

Van Campo, E., Cour, P., Huang, S., 1996. Holocene environmental changes in Bangong Co basin (Western Tibet), part 2: the pollen record. Palaeogeogr. Palaeoclimatol. Palaeoecol. 120, 49–63.

Wang, R.L., Scarpitta, S.C., Zhang, S.C., Zheng, M.P., 2002. Later Pleistocene/Holocene climate conditions of Qinghai–Xizhang Plateau (Tibet) based on carbon and oxygen stable isotopes of Zabuye Lake sediments. Earth Planet. Sci. Lett. 203, 461–477.

Webster, P.J., Yang, S., 1992. Monsoon and ENSO: selectively interactive systems. Q. J. R. Meteorol. Soc. 118, 877–926.

Werner, M., Langebroek, P.M., Carlsen, T., Herold, M., Lohmann, G., 2011. Stable water isotopes in the ECHAM5 general circulation model: toward high-resolution isotope modeling on a global scale. J. Geophys. Res., Atmos. 116, D15109.

Wischnewski, J., Mischke, S., Wang, Y., Herzschuh, U., 2011. Reconstructing climate variability on the northeastern Tibetan Plateau since the last lateglacial – a multi-proxy, dual-site approach comparing terrestrial and aquatic signals. Quat. Sci. Rev. 30, 82–97.

Wu, Y., Luecke, A., Jin, Z., Sumin, W., Schleser, G.H., Battarbee, R.W., Xia, W., 2006. Holocene climate development on the central Tibetan Plateau: a sedimentary record from Cuoe Lake. Palaeogeogr. Palaeoclimatol. Palaeoecol. 234, 328–340.

Wuennemann, B., Mischke, S., Chen, F., 2006. A Holocene sedimentary record from Bosten lake, China. Palaeogeogr. Palaeoclimatol. Palaeoecol. 234, 223–238.

Yao, T., Masson-Delmotte, V., Gao, J., Yu, W., Yang, X., Risi, C., Sturm, C., Werner, M., Zhao, H., He, Y., Ren, W., Tian, L., Shi, C., Hou, S., 2013. A review of climatic controls on in $\delta^{18}O$ precipitation over the Tibetan Plateau: observations and simulations. Rev. Geophys. 51, 525–548. http://dx.doi.org/10.1002/rog.20023.

Yu, L., Lai, Z., 2014. Holocene climate change inferred from stratigraphy and OSL chronology of Aeolian sediments in the Qaidam Basin, northeastern Qinghai–Tibetan Plateau. Quat. Res. 81, 488–499.

Zhang, C., Mischke, S., 2009. A lateglacial and Holocene lake record from the Nianbaoyeze Mountains and inferences of lake, glacier and climate evolution on the eastern Tibetan Plateau. Quat. Sci. Rev. 28, 1970–1983.

Zhang, J., Chen, F., Holmes, J.A., Li, H., Guo, X., Wang, J., Li, S., Lue, Y., Zhao, Y., Qiang, M., 2011. Holocene monsoon climate documented by oxygen and carbon isotopes from lake sediments and peat bogs in China: a review and synthesis. Quat. Sci. Rev. 30, 1973–1987.

Zheng, Y.Q., Yu, G., Wang, S.M., Xue, B., Zhuo, D.Q., Zeng, X.M., Liu, H.Q., 2004. Simulation of paleoclimate over East Asia at 6 ka BP and 21 ka BP by a regional climate model. Clim. Dyn. 23, 513–529. http://dx.doi.org/10.1007/s00382-004-0452-7.

Zhou, W., Lu, X., Wu, Z., Deng, L., Jull, A.J.T., Donahue, D.J., Beck, W., 2002. Peat record reflecting Holocene climate change in the Zoige Plateau and AMS radiocarbon dating. Chin. Sci. Bull. 47, 66–70.